Chinese Journal of Aeronautics, (2018), 31(5): 927–940

Chinese Society of Aeronautics and Astronautics
& Beihang University

Chinese Journal of Aeronautics

cja@buaa.edu.cn
www.sciencedirect.com

Modeling and analysis of mover gaps in tubular moving-magnet linear oscillating motors

Xuesong LUO [a], **Chao ZHANG** [a,*], **Shaoping WANG** [a], **Enrico ZIO** [b], **Xingjian WANG** [a]

[a] *School of Automation Science and Electrical Engineering, Beihang University, Beijing 100083, China*
[b] *Energy Department-Nuclear Section, Polytechnic of Milan, Via Ponzio 34/3, I-20133 Milan, Italy*

Received 20 January 2017; revised 14 March 2017; accepted 12 April 2017
Available online 14 November 2017

KEYWORDS

Air-gap flux density;
Linear motor;
Mover gaps;
Quasi-Halbach array;
Thrust output;
Tubular moving-magnet linear oscillating motor (TMMLOM)

Abstract A tubular moving-magnet linear oscillating motor (TMMLOM) has merits of high efficiency and excellent dynamic capability. To enhance the thrust performance, quasi-Halbach permanent magnet (PM) arrays are arranged on its mover in the application of a linear electro-hydrostatic actuator in more electric aircraft. The arrays are assembled by several individual segments, which lead to gaps between them inevitably. To investigate the effects of the gaps on the radial magnetic flux density and the machine thrust in this paper, an analytical model is built considering both axial and radial gaps. The model is validated by finite element simulations and experimental results. Distributions of the magnetic flux are described in condition of different sizes of radial and axial gaps. Besides, the output force is also discussed in normal and end windings. Finally, the model has demonstrated that both kinds of gaps have a negative effect on the thrust, and the linear motor is more sensitive to radial ones.

1. Introduction

Tubular moving-magnet linear oscillating motors (TMMLOMs) are specific linear actuators that produce a high-frequency reciprocating motion. Their outstanding characteristics, such as efficiency, dynamic performance, and simple structure, give their broad application prospect, but their model has not been clearly described and their structure has not been optimized adequately. TMMLOMs work at a designed frequency with the stroke of mover oscillating no more than one pole pitch, which are widely applied in many equipment, such as artificial hearts, compressors, refrigerators, etc.[1–5] As short-travel actuations are propelled directly without conventional cranks, TMMLOMs enjoy a 20%-30% better efficiency compared with rotary motors in the application of household refrigerator compressors.[5] By enlarging the power whilst reducing acoustic noise and vibrations accordingly, TMMLOMs are tested for air-conditioner compressors with an efficiency of over 92% at a rated condition.[6] Due to a relatively higher frequency response benefited from the absence

* Corresponding author.
E-mail address: czhangstar@gmail.com (C. ZHANG).

Peer review under responsibility of Editorial Committee of CJA.

ELSEVIER Production and hosting by Elsevier

https://doi.org/10.1016/j.cja.2017.11.008

of rotor inertia in the rotary mechanism, TMMLOMs are developed to drive the servo pump in a hydraulic system.[7] Meanwhile, TMMLOMs are utilized in linear electro-hydrostatic actuators in more-electric aircraft systems with a high power density.[8] In addition, a cooperative configuration is introduced where two movers of dual TMMLOMs work with a phase angle of $\pi/2$.[9] A reliable coordinated control of two TMMLOMs requires a regulation based on an accurate model. Furthermore, a powerful output with limited space and restricted mass in aircraft also needs more optimized analysis of the motor structure and principle based on a precise calculation of the air-gap magnetic field. A comprehensive model, therefore, is indispensable for TMMLOMs.

Some well-known modeling optimization approaches, such as changing the direction of magnetization on a mover, configuring the groups of PM arrays on movers, decreasing the slots of the stator, and regulating the split ratio of E-Core PMs, have been confirmed to improve the characteristics of TMMLOMs. However, current research pays little attention to the effects of mover gaps (air gaps among PMs or between PMs and materials) which exist inherently in the segments of PMs. Despite the fact that the effects of discontinuity on PMs has not been proven to be very prominent, an introduction of their effects on the distribution of a magnetic field through an analytical mathematics and simulation model is also a necessity when aiming to optimize a TMMLOM for a high-performance aeronautical facility and create a dual-motor collaborative control strategy on this basis.

Many studies about the TMMLOMs have been published over the last three decades, focusing on improving the output performance analytically and experimentally through reducing the mover weight and increase the frequency.[3,4]

The topology of PMs is an important factor that influences the output performance. Kim et al. proposed a linear oscillatory actuator whose magnetization direction of PMs was parallel to the stroke axis,[10] and the machine shared a high-power density and a low-cogging force. A transient model of this motor was validated experimentally.[11] In the contrary, Kim et al. discussed a TMMLOM with its magnetization direction perpendicular to the motion direction.[12,13] The magnetic field was analyzed by an analytical model, and the prototype gave capabilities of high force density and low detent force. By the ways of magnetic vector potential and cylindrical coordinate formulation, Wang et al. presented a general framework for TMMLOMs. His solutions presented the analytical field distribution for both axial polarized and radial polarized tubular linear PM motors.[14] The air-gap flux densities of both topologies were compared,[15] and a finite element model showed that the radial attractive force was higher in the axial polarized structures when considering the eccentricity effect.

In a publication series presented by Wang et al., a quasi-Halbach structure of TMMLOMs which was a combination of radial polarized and axial polarized PMs arrays was deeply analyzed,[14,16–19] including an analytical flux expression of the quasi-Halbach topology,[14,16,18] comparative analysis to conventional magnetization methods,[17] and parameters optimizations on the size of the structure.[19] Because of some self-shielding property, the quasi-Halbach PM arrays would reduce the moving mass to improve the dynamic capability and result in a higher flux density.

The coupling between windings and PMs is another area that researchers have focused on. Considering the configuration of stator windings in TMMLOMs, Wang et al. deduced a set of formulations to describe the distribution of magnetic flux theoretically based on Maxwell's equations.[16] Zhu et al. studied a variety of winding arrangements with a PMs assembly.[20–24] A rule was outlined that the stator tooth number was supposed to differ the mover pole number by 1 in TMMLOMs.[20] Subsequently, simulation calculations and experiment validations were finished by Zhu et al., which demonstrated that the E-core wind configuration yielded less flux leakage and performed conducive to the oscillation.[20,22] Eventually, design optimization and prototype validation was implemented for the topology of a TMMLOM with E-type windings and quasi-Halbach PMs.[23,24] This type of motor was further extended into E-type series TMMLOMs,[25] which consisted of multi-pair E-cores with a quasi-Halbach topology to enhance the thrust. Furthermore, Jiao et al. presented compound Halbach PMs in a TMMLOM, whose topology was a dual-layer integration of quasi-Halbach PMs and axial polarized PMs.[26] In Jiao's structure, the conventional back-iron was not needed any more, hence the mover mass could be decreased further with a better dynamic performance.

To improve the properties of a TMMLOM, a stator slot was taken into account by researchers. Bianchi et al. analyzed the factor of a stator slot that affected the force.[15] His research showed that slotless motors shared a higher mean force than slotted ones. Kim et al. designed a slotted TMMLOM[13] and a slotless TMMLOM[12] for an eco-pedal system, and the later presented a smaller force ripple experimentally. An analytical model with a quasi-Halbach magnetized armature and a semi-closed slot stator was given by Chen et al.,[23] and a closed slot structure was employed into a TMMLOM to reduce the cogging force in Liang's paper,[7] of which the leakage permeability was much larger than that of the former. Besides, Kim et al. proposed a novel method for stator lamination to laminate the teeth and yoke of a stator respectively, which decreases the gaps in the stator and multiplies the flux density.

By introducing a Carter coefficient, Wang et al. modified the analytical model of tubular linear PM motors with a slotted stator[14] and a semi-closed slotted stator.[27] They also applied this correction to calculate the distribution of flux density of a TMMLOM with quasi-Halbach PMs. This method was also followed by Wang et al. to model the E-type series TMMLOMs.[28]

Experimental, numerical, and analytical methods are the three normal research approaches on LMMLOM research. Some studies have been implemented entirely experimentally,[6,10,29,30] whose results could exhibit the performance of a motor directly. However, they didn't reveal the principle of LMMLOMs. Numerical approaches have been widely applied in LMMLOM designs,[7,17,31–35] which allow to solve a complex design without much approximation. However, it didn't reflect the relation between topological parameters and the motor performance, which results in a difficulty in optimization.

The key step to model a TMMLOM is to describe the distribution of magnetic flux, resulting from which that analytical methods can be grouped into three categories. One is lumped magnetic circuit models,[7,24,36–38] which consider a motor made of several parts with individual magnetic parameters, and they can only model the motor roughly due to the lumped approximation method. Another choice is the equivalent surface current method, which introduces several layers of surface current to take the place of PMs.[37] Its approximate structure can only

outline the regularities of PMs with a simple geometric form. The last one is the analytical solution from Maxwell's equations,[16,18,23,25,28] that shares a better approximation of the real magnetic flux. It is restricted that indispensable approximate conditions need be set to ensure the model solvable.

An accurate model depends on the numbers of factors which should be taken into account during modeling. Most of the literature studied TMMLOMs, and took the configurations of mover PMs and stator topology into consideration. The flux density in the air-gap determines the output capacity of the motor. A quasi-Halbach PMs array proves its better performance in the flux density due to the self-shielding property, and its model has been analyzed in detail.[16–24,28] It produces a larger flux distribution with an equal mover mass, which can increase properties of both thrust and dynamic. Reduction of the stator slot, in addition, is also an effective approach to improve the flux distribution, whose model has also drawn a lot of focus from researchers,[7,14,15,17,23,26,27] because permeability is quite sensitive to air medium.

Air medium also exists in the mover of a TMMLOM, the surface of which is assembled by several individual PM modules. The manufacturing method results in some gaps among PM arrays as well as between PMs and the mover frame. Bianchi analyzed that the magnetic flux could move through the small air-gap in an axial magnetized mover causing a radial force.[15] However, he just focused on the radial force in a TMMLOM by the method of finite element and didn't give a model to explain how the gaps affected the flux distribution. Via analytical analysis,[39] Xia et al. presented the negative influence caused by gaps between Halbach PM segments in rotary motors, discussing the relationship between the effect of gaps and the parameters of PMs through an analytical model. In Xia's paper, however, the gaps were only investigated in a circumferential dimension. Similar to rotary motors, mover gaps also exist in linear motors as well as TMMLOMs, whose gaps are more complex than those of rotary machines because of a more complex structure in the mover. The surface of the mover is mounted by PM segments including radial polarized ones and axial polarized ones. Due to the installation error, the stuffed glue, and the interaction force among PMs, gaps are inevitable between and beneath segments in quasi-Halbach arrays. The existence of gaps would affect the magnetic flux distribution and output thrust. Therefore, the thrust model of TMMLOMs considering mover gaps is a necessity for designing a high-precision control strategy.

In this paper, Section 1 introduces the problem statement of TMMLOMs. Section 2 establishes a modeling method considering the mover gaps. Section 3 gives model validation and performance analysis. Finally, conclusions are presented in Section 4.

2. Schematic structure

In this section, the structure of a TMMLOM is clarified for further understanding. Subsequently, the existence of gaps in the mover is presented in detail.

2.1. Structure of a TMMLOM

The structure of a TMMLOM consisting of 4 pairs of E-type windings with a quasi-Halbach PMs configuration is shown in Fig. 1. The Matierial of PMs is NdFeB N38SH. Silicon steel is laminated circumferentially to make up the stator core, and coils are connected in parallel through the stator, while the hollow mover is made of electrical iron with PMs covered on the surface. Including radial polarized PMs and axial polarized PMs, a quasi-Halbach array can enhance the magnetic flux over the outer surface of the mover resulting from its self-shielding effect. The stroke of this machine is designed to be 5 mm in maximum.

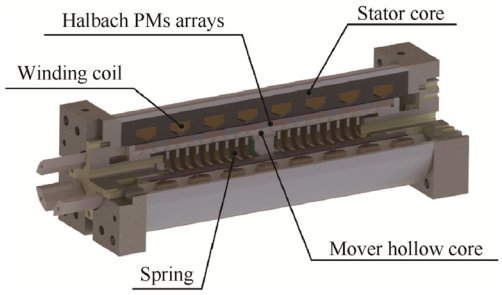

Fig. 1 Structure of a TMMLOM.

The hollow core lightens the mover mass, which enables the TMMLOM to work at a high frequency of 100 Hz. Moreover, this design also improves the dynamic performance. High power and good dynamic response make it possible to meet the requirements of an aircraft actuator.

2.2. Gap topology

As shown in Fig. 2 and Fig. 3, all the individual PM segments assembled on the mover core can be classified into two types. An axial polarized PM segment is a torus whose magnetization direction is along the z-axis. A radial polarized PM segment is a radial magnetized one, which was fabricated with a tile-like shape as well as a central angle of 60°

Gaps are very clear between these segments as marked in Fig. 2. In the installation process of Quasi-Halbach arrays, the adhesive would take up less room inevitably between PMs. In addition, the design tolerance as well as the interaction force between segments will also account for the assembly gaps. For the permeability in non-ferromagnetic gaps is different from that in ferromagnetic ones, the existence of gaps will affect the distribution of the magnetic flux. Allowing for the structure of Quasi-Halbach segments, the gaps mentioned above can be divided into three categories, i.e., radial gaps, axial gaps, and circumferential gaps, which are illustrated in Fig. 3. x, y, z are three axes in Cartesian coordinate system and r, θ, z are axes in cylindrical coordinate system, where $\boldsymbol{e}_{\mathrm{ra}}$, $\boldsymbol{e}_{\mathrm{ci}}$, $\boldsymbol{e}_{\mathrm{ax}}$ are the unit vectors in radial, circumferential and

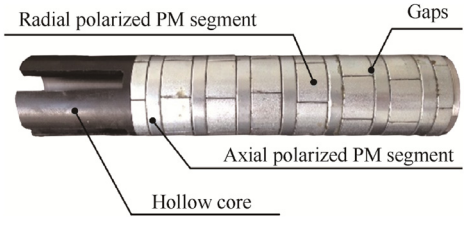

Fig. 2 Mover prototype.

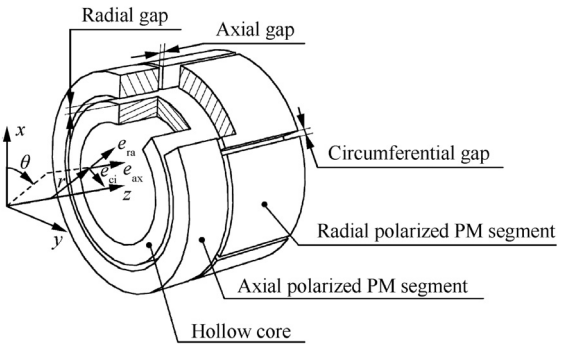

Fig. 3 Mover structure.

axial directions respectively. Radial gaps exist between PMs and the hollow core, axial gaps between axial polarized PMs and radial polarized PMs, and circumferential gaps between tile-like PMs. The three kinds of gaps have individual effects on the magnet flux, and subsequently, the characteristics of radial and axial gaps are about to be discussed in the following section.

3. Mathematical model considering mover gaps

In this section, an analytical model is yielded in cylindrical coordinates by the method of magnetization vector. Based on Laplace's and Poisson's equations, radial and axial gaps are taken into consideration. Moreover, boundary conditions are presented and the distribution of the magnetic flux is deduced in the air-gap. On this basis, an output thrust model is given.

3.1. Model assumption and magnetization vector

To research the effect of gaps in the mover on the air-gap magnetic field, it's necessary to build an analytical model considering the gaps, and in order to simplify the derivation of the analytical model, some assumptions are stated here.

(1). The axial length of the theoretical model is infinite. It comprises a series of repetitive permanent magnet armatures in the TMMLOM extending to infinity, which facilitates a Fourier series representation, and the cycle length is much longer than the length of the motor.
(2). Each individual permanent magnet shares the same size and magnetic property with a smooth surface, and the gaps of the same type have the same thickness.
(3). The analytical model ignores the saturation phenomenon.
(4). A Carter coefficient will be introduced to compensate the impact of the stator slot.
(5). The stator and the hollow core are infinitely permeable while the relative permeability of PMs is approximated as 1.

In formulation of the magnetic field, the room to be studied is divided into the following three regions based on magnetic characteristics, as shown in Fig. 4.

(1). Region I is the space of the air-gap.
(2). Region II denotes the permanent magnets arrays filled with a rare-earth magnetic material with axial gaps.
(3). Region III represents the radial gaps between the permanent magnets and the hollow core.

g_{ra} and g_{ax} are radial and axial gap in Fig. 4, τ_w the width of stator winding, b_t the width of stator teeth, g the length of air-gap, τ_{ra} length of radially magnetized PMs, τ_{ax} length of axially magnetized PMs, τ_p the pole pitch, R_s the outer radius of mover, R_h the outer radius of mover hollow core and R_{sh} the inner radius of mover hollow core. The magnetic field properties in the three regions are characterized by an expression between the magnetic field intensity $\boldsymbol{H}_I$, $\boldsymbol{H}_{II}$, $\boldsymbol{H}_{III}$ (in A/m) and the magnetic flux density $\boldsymbol{B}_I$, $\boldsymbol{B}_{II}$, $\boldsymbol{B}_{III}$ (in Tesla) as

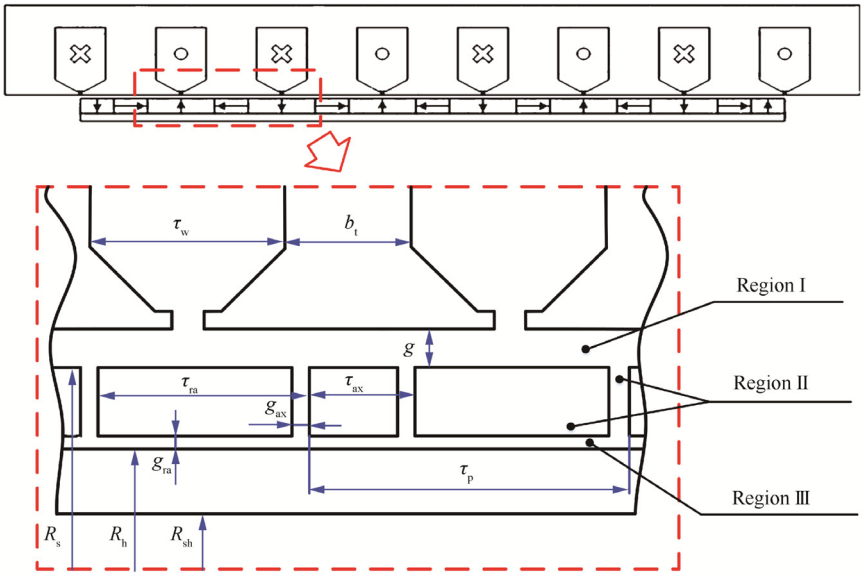

Fig. 4 Magnets topology and leading parameters of TMMLOM.

$$\begin{cases} \boldsymbol{B}_{\mathrm{I}} = \mu_0 \boldsymbol{H}_{\mathrm{I}} \\ \boldsymbol{B}_{\mathrm{II}} = \mu_0 \mu_{\mathrm{rII}} \boldsymbol{H}_{\mathrm{II}} + \mu_0 \boldsymbol{M}_0 \\ \boldsymbol{B}_{\mathrm{III}} = \mu_0 \boldsymbol{H}_{\mathrm{III}} \end{cases} \tag{1}$$

where μ_0 is the permeability of vacuum with a value of $4\pi \times 10^{-7}$ H/m, μ_{rII} the relative permeability of PMs, and $\boldsymbol{M}_0$ the residual magnetization vector in A/m.

The magnetization vector $\boldsymbol{M}$ of the PMs array can be expressed in the cylindrical coordinates as

$$\boldsymbol{M} = M_{\mathrm{ra}} \boldsymbol{e}_{\mathrm{ra}} + M_{\mathrm{ax}} \boldsymbol{e}_{\mathrm{ax}} \tag{2}$$

where M_{ra} is the radial components of the magnetization vector, M_{ax} the axial components of the magnetization vector. Their spatial distributions are shown in Fig. 5 where M_0 is the absolute value of magnetization vector which is given by

$$M_0 = \frac{B_{\mathrm{re}}}{\mu_0} \tag{3}$$

where B_{re} is the magnet remanence of permanent magnets. Equations of M_{ra} and M_{ax} derived from the configuration of PMs as shown in Fig. 5, where R_{se} is the effective stator inner radius, R_{m} is the effective PMs inner radius, and R_{p} is the effective hollow core outer radius .

They can be resolved into Fourier series, which are given by

$$\begin{cases} M_{\mathrm{ra}} = \sum_{k=1}^{\infty} a_k \cos(m_k z) \\ M_{\mathrm{ax}} = \sum_{k=1}^{\infty} b_k \sin(\mathrm{m}_k \mathrm{z}) \end{cases} \tag{4}$$

where $m_k = \frac{2k\pi}{\tau_{\mathrm{lp}}}$, $z$the axial position, and τ_{lp} the cycle length utilized in the Fourier series. Define that $C_{\mathrm{ax1}} = \frac{\tau_{\mathrm{ra}} - g_{\mathrm{ax}}}{2}$ and $C_{\mathrm{ax2}} = \frac{\tau_{\mathrm{ra}} + g_{\mathrm{ax}}}{2}$, and the coefficients are determined as

$$\begin{cases} a_k = \frac{2B_{\mathrm{re}}}{\mu_0 k\pi} \{ -\sin(m_k C_{\mathrm{ax1}}) + \sin(m_k \tau_{\mathrm{p}}) - \sin[m_k(\tau_{\mathrm{p}} - C_{\mathrm{ax1}})] \} \\ b_k = \frac{2B_{\mathrm{re}}}{\mu_0 k\pi} \{ \cos(m_k C_{\mathrm{ax2}}) - \cos[m_k(\tau_{\mathrm{p}} - C_{\mathrm{ax2}})] \} \end{cases} \tag{5}$$

3.2. Distribution of flux density

According to the fundamental theory of an electromagnetic field, the magnetic field in the TMMLOM is a solenoid field or source-free field, namely,

$$\nabla \cdot \boldsymbol{B}_i = \boldsymbol{0} \tag{6}$$

where $i = \mathrm{I}, \mathrm{II}, \mathrm{III}$ that represent the three regions. It can be derived that for any vector, the divergence of its curl is always equal to zero. Thus, a magnetic vector potential $\boldsymbol{A}_i$ in region i can be introduced, so that

$$\boldsymbol{B}_i = \nabla \times \boldsymbol{A}_i \tag{7}$$

Furthermore, deducing from Appendix A, the governing equations in the three regions are obtained as

$$\begin{cases} \nabla^2 \boldsymbol{A}_{\mathrm{I}} = \boldsymbol{0} \\ \nabla^2 \boldsymbol{A}_{\mathrm{II}} = -\mu_0 \nabla \times \boldsymbol{M} \\ \nabla^2 \boldsymbol{A}_{\mathrm{III}} = \boldsymbol{0} \end{cases} \tag{8}$$

The magnetic vector potential in cylindrical coordinates can be expressed as

$$\boldsymbol{A}_i = A_{i,\mathrm{ra}} \boldsymbol{e}_{\mathrm{ra}} + A_{i,\mathrm{ci}} \boldsymbol{e}_{\mathrm{ci}} + A_{i,\mathrm{ax}} \boldsymbol{e}_{\mathrm{ax}} \tag{9}$$

where $A_{i,\mathrm{ra}}$ is the radial component of $\boldsymbol{A}_i$, $A_{i,\mathrm{ci}}$ the circumferential component of $\boldsymbol{A}_i$ and $A_{i,\mathrm{ax}}$ the axial component of $\boldsymbol{A}_i$. For the magnetic field distribution of a tubular linear oscillating motor is axially symmetric, $\boldsymbol{A}_i$ has only one component $A_{i,ci}$. Therefore, the governing equations can be transformed into

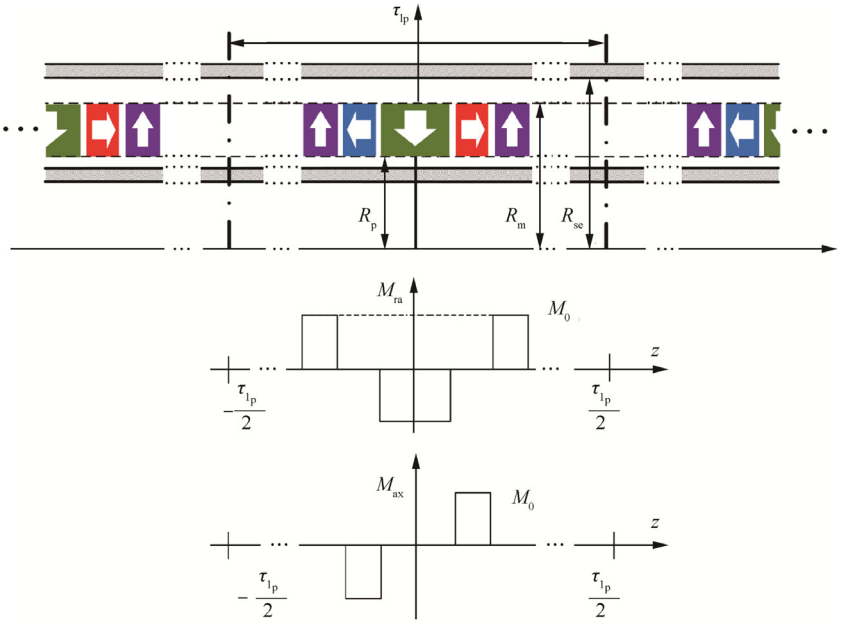

Fig. 5 Distribution of magnetization vector.

$$\begin{cases} A_{\mathrm{I,ci}} = \sum_{k=1}^{\infty}\{[a_{\mathrm{I},k}I_1(m_k r) + b_{\mathrm{I},k}K_1(m_k r)]\sin(m_k z)\} & \text{(region I)} \\ A_{\mathrm{II,ci}}, = \sum_{k=1}^{\infty}[a_{\mathrm{II},k}I_1(m_k r) + b_{\mathrm{II},k}K_1(m_k r) + P_k L_1(m_k r)]\sin(m_k z) & \text{(region II)} \\ A_{\mathrm{III,ci}} = \sum_{k=1}^{\infty}\{[a_{\mathrm{III},k}I_1(m_k r) + b_{\mathrm{III},k}K_1(m_k r)]\sin(m_k z)\} & \text{(region III)} \end{cases} \tag{10}$$

where $P_k = \frac{\mu_0 \pi a_k}{2m_k}$, $a_{\mathrm{I},k}, b_{\mathrm{I},k}, a_{\mathrm{II},k}, b_{\mathrm{II},k}, a_{\mathrm{III},k}, b_{\mathrm{III},k}$ are constants and r is the radial position. $I_n(x)$ and $K_n(x)$ are the modified Bessel functions of the first and second kinds of order n, respectively, which are defined as

$$\begin{cases} I_n(x) = \sum_{m=0}^{\infty} \frac{1}{m!\Gamma(m+n+1)}\left(\frac{x}{2}\right)^{2m+n} \\ K_n(x) = \frac{\pi}{2}\cdot\frac{I_{-n}(x) - I_n(x)}{\sin(n\pi)} \end{cases} \quad x \in \mathrm{C} \tag{11}$$

The detailed formulas and the expression of $L_{\mathrm{n}}(x)$ are presented in Appendix B. According to Eqs. (1) and (7), the distribution of the magnet field is given as follows.

$B_{i,\mathrm{ra}}$, $B_{i,\mathrm{ax}}$ are the radial and axial component of $\boldsymbol{B}_i$ in region i, $H_{i,\mathrm{ra}}$, $H_{i,\mathrm{ax}}$ are the radial and axial component of $\boldsymbol{H}_i$ in region i. In regions I and III,

$$\begin{cases} B_{i,\mathrm{ra}} = \sum_{k=1}^{\infty}\{-m_k[a_{i,k}I_1(m_k r) + b_{i,k}K_1(m_k r)]\cos(m_k z)\} \\ B_{i,\mathrm{ax}} = \sum_{k=1}^{\infty}\{m_k[a_{i,k}I_0(m_k r) - b_{i,k}K_0(m_k r)]\sin(m_k z)\} \\ H_{i,\mathrm{ra}} = \sum_{k=1}^{\infty}\left\{-\frac{m_k}{\mu_0}[a_{i,k}I_1(m_k r) + b_{i,k}K_1(m_k r)]\cos(m_k z)\right\} \\ H_{i,\mathrm{ax}} = \sum_{k=1}^{\infty}\left\{\frac{m_k}{\mu_0}[a_{i,k}I_0(m_k r) - b_{i,k}K_0(m_k r)]\sin(m_k z)\right\} \end{cases} \tag{12}$$

where i = I, III. In region II,

$$\begin{cases} B_{\mathrm{II,ra}} = \sum_{k=1}^{\infty}\{-m_k[a_{\mathrm{II},k}I_1(m_k r) + b_{\mathrm{II},k}K_1(m_k r) + P_k L_1(m_k r)]\cos(m_k z)\} \\ B_{\mathrm{II,ax}} = \sum_{k=1}^{\infty}\{m_k[a_{\mathrm{II},k}I_0(m_k r) - b_{\mathrm{II},k}K_0(m_k r) + P_k L_0(m_k r)]\sin(m_k z)\} \\ H_{\mathrm{II,ra}} = \sum_{k=1}^{\infty}\left\{-\frac{m_k}{\mu_0}[a_{\mathrm{II},k}I_1(m_k r) + b_{\mathrm{II},k}K_1(m_k r) + P_k L_1(m_k r) + \frac{\mu_0 a_k}{m_k}]\cos(m_k z)\right\} \\ H_{\mathrm{II,ax}} = \sum_{k=1}^{\infty}\left\{\frac{m_k}{\mu_0}[a_{\mathrm{II},k}I_0(m_k r) - b_{\mathrm{II},k}K_0(m_k r) + P_k L_0(m_k r) - \frac{\mu_0 b_k}{m_k}]\sin(m_k z)\right\} \end{cases} \tag{13}$$

In the TMMLOM, the magnetic flux density is continuous in the normal direction of the interface between two mediums, while the magnetic field intensity continuous in the tangential direction. Accordingly, boundary conditions are given as

$$\begin{cases} H_{\mathrm{I,ax}}|_{r=R_{\mathrm{se}}} = 0 \\ B_{\mathrm{I,ra}}|_{r=R_{\mathrm{m}}} = B_{\mathrm{II,ra}}|_{r=R_{\mathrm{m}}} \\ H_{\mathrm{I,ax}}|_{r=R_{\mathrm{m}}} = H_{\mathrm{II,ax}}|_{r=R_{\mathrm{m}}} \\ B_{\mathrm{II,ra}}|_{r=R_{\mathrm{p}}} = B_{\mathrm{III,ra}}|_{r=R_{\mathrm{p}}} \\ H_{\mathrm{II,ax}}|_{r=R_{\mathrm{p}}} = H_{\mathrm{III,ax}}|_{r=R_{\mathrm{p}}} \\ H_{\mathrm{III,ax}}|_{r=R_{\mathrm{h}}} = 0 \end{cases} \tag{14}$$

The compensation of the stator slot in the TMMLOM is accounted for by introducing a Carter coefficient K_{c},[40] and the equations is given as follows:

$$\begin{cases} g' = g + R_{\mathrm{s}} - R_{\mathrm{h}} \\ \gamma = \frac{4}{\pi}\left[\frac{\tau_{\mathrm{p}} - b_{\mathrm{t}}}{2g'}\tan^{-1}\left(\frac{\tau_{\mathrm{p}} - b_{\mathrm{t}}}{2g'} - \ln\sqrt{1 + \left(\frac{\tau_{\mathrm{p}} - b_{\mathrm{t}}}{2g'}\right)^2}\right)\right] \\ K_{\mathrm{c}} = \frac{\tau_{\mathrm{p}}}{\tau_{\mathrm{p}} - \gamma g'} \end{cases} \tag{15}$$

Therefore, the effective air-gap g_{e}, the effective stator inner radius R_{se}, the effective PMs inner radius R_{m} and the effective hollow core outer radius R_{p} are deduced as follows:

$$\begin{cases} g_{\mathrm{e}} = g + (K_{\mathrm{c}} - 1)g' \\ R_{\mathrm{se}} = R_{\mathrm{s}} + (K_{\mathrm{c}} - 1)g' \\ R_{\mathrm{m}} = R_{\mathrm{s}} \\ R_{\mathrm{p}} = R_{\mathrm{h}} + g_{\mathrm{ra}} \end{cases} \tag{16}$$

Utilizing the expressions of $a_{\mathrm{I},k}, b_{\mathrm{I},k}, a_{\mathrm{II},k}, b_{\mathrm{II},k}, a_{\mathrm{III},k}, b_{\mathrm{III},k}$ in Appendix C, the distribution of the magnetic flux can be determined uniquely.

3.3. Models of electromotive force and thrust

As shown in Fig. 6, z_{d} is the travel distance of the mover, and the configuration of coils is composed of 4 pairs of windings. In terms of the positions of windings, the coils region can be

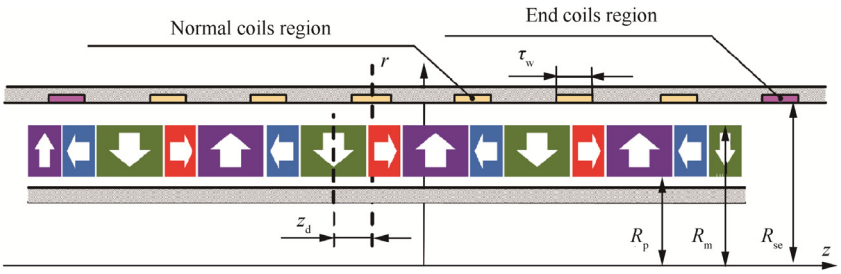

Fig. 6 Topology of an armature.

divided into two categories. One is the normal coils winding whose arrangement is next to two other windings. The other one is the end coils winding which is located at the end of the TMMLOM. Moreover, the flux-linkage of a single winding Ψ_c can be deduced by integration as

$$\Psi_c = \frac{N_c}{\tau_w}\int_{z_d-\frac{\tau_w}{2}}^{z_d+\frac{\tau_w}{2}} 2\pi R_{se} A_{1,ci}(R_{se}, z)\mathrm{d}z \tag{17}$$

where N_c is the number of coils turns in a single winding region.

Applying the flux distribution of a normal coils region calculated before to Eq. (17) yields

$$\Psi_c = 2\pi\sum_{k=1}^{\infty}\left[\frac{K_{Wk}K_{Sk}}{m_k}\sin(m_k z_d)\right] \tag{18}$$

where

$$K_{Wk} = \frac{N_c \sin\left(m_k\frac{\tau_w}{2}\right)}{m_k\frac{\tau_w}{2}} \tag{19}$$

$$K_{Sk} = m_k R_{se}[a_{1,k}I_1(m_k R_{se}) + b_{1,k}K_1(m_k R_{se})] \tag{20}$$

K_{Wk} reflects the influence of the windings configuration, and the more turns that coils are arranged in the width, the better output the TMMLOM performs, while K_{Sk} is a parameter that contains the information of the structure of an armature and the topology of PMs. When neglecting the magnetic saturation effects, K_{Sk} keeps constant. Hence, the electromotive force of a single winding can be given by

$$e_c = -\frac{\mathrm{d}\Psi_c}{\mathrm{d}t} = -2\pi v\sum_{k=1}^{\infty}[K_{Wk}K_{Sk}\cos(m_k z_d)] \tag{21}$$

where v is the instantaneous speed of the mover. Thus, the thrust of a normal coil F_c is obtained as

$$F_c = \frac{e_c i}{v} = -2\pi i\sum_{k=1}^{\infty}[K_{Wk}K_{Sk}\cos(m_k z_d)] \tag{22}$$

in which i is the instantaneous current in a single winding. In terms of the end coils, the thrust F_{ec} is expressed by

$$F_{ec} = -2\pi i\sum_{k=1}^{\infty}\{K_{Wk}K_{Sk}\cos[m_k(z_d+\tau_p)]\} \tag{23}$$

As the TMMLOM has 6 normal coils windings and 2 end coils windings, the total thrust F is derived finally as follows:

$$F = -2\pi i\sum_{k=1}^{\infty}\{K_{Wk}K_{Sk}[6\cos(m_k z_d) + 2\cos(m_k z_d) \times \cos(m_k\tau_p)]\} \tag{24}$$

After the design finalization of the TMMLOM, Eq. (24) indicates that the thrust is a function of the current and the mover position.

4. Simulation and validation

In this section, analytical calculations and FEM experiments are implemented based on the major parameters of the TMMLOM given in Table 1, and the model is validated by measured results.

4.1. Validation of the analytical model

Finite element model (FEM) analysis achieves a good accuracy in the magnetic flux distribution of a tubular linear motor.[41] To verify the analytical model proposed in the last section, an FEM is established in the ANSYS Maxwell software. The open-circuit magnetic field whose coils are not energized is simulated, and the flux density distributed in the air-gap is generated by a quasi-Halbach PM arrays form mover. The radial flux density at the radius of r = 18.3 mm is illustrated in Fig. 7 (a) and the axial flux density in Fig. 7(b). The calculated results from the analytical model are also depicted in both figures as well. As shown in Fig. 7(a), the analytical results matches well with the red curves, which is precise enough to describe the flux regularity and calculate the output thrust.

Besides, the axial flux density obtained from the analytical results also shares a similar trend to the FEM data, and the practicability of the proposed model has been demonstrated.

The output force of the TMMLOM is related to the distribution of the radial density. According to the axial information of flux calculated above, the thrust can be derived analytically. The analytical relations and finite element results are exhibited in Fig. 8.

Table 1 Leading parameters of the TMMLOM.

Symbol	b_t (mm)	τ_w (mm)	g (mm)	τ_{ra} (mm)	τ_{ax}(mm)	τ_p (mm)	R_{sh} (mm)	R_h (mm)	R_s (mm)	B_{re} (T)
Value	12	3	1	16	8	24	10	14	18	1.24

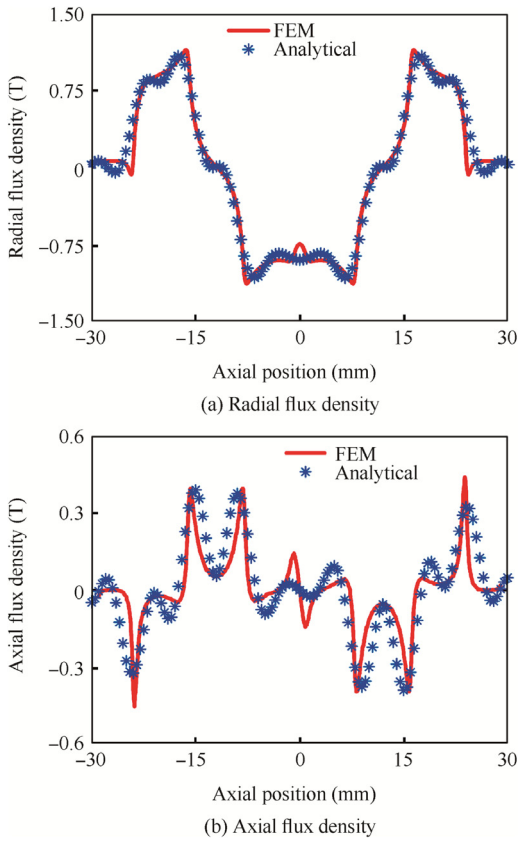

Fig. 7 Validation of flux density.

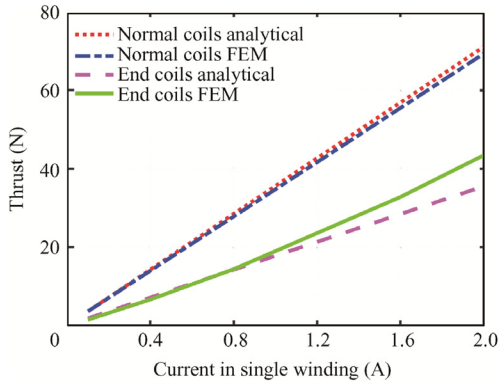

Fig. 8 Validation of thrust.

It can be validated that the normal coils and end coils have different regulations of output force. The normal coils, which produce the thrust primarily, fit very well with the FEM result. It is demonstrated that the thrust of the normal coils is a linear function to the current, and the small error in condition of high current is caused by the magnetic saturation. The end coils model, however, presents a larger error. Because the end effect of the liner motor, the magnetic flux is unsymmetrical with respect to the end coils. Due to the fact that the TMMLOM has 6 normal coils windings and only 2 end coils windings, what's more, the force generated by the end coils is only half of that by the normal coils. Hence, the error is acceptable, and the thrust model is suitable in gap analysis.

4.2. Effect of the radial and axial gaps

4.2.1. Effect of the radial and axial gaps on the flux distribution

After validation of the proposed model considering the mover gaps, the effect of gaps is discussed. For the radial magnetic flux is a key factor that affects the output, the distribution of the magnetic flux in the radial direction is analyzed considering radial gaps in Fig. 9(a) and axial gaps in Fig. 9(b), respectively.

Fig. 9(a) shows the distribution of the radial flux in the air-gap with different sizes of radial gaps. It demonstrates that radial gaps would decrease the amplitude comprehensively. Even though they do not change the waveform of the flux distribution, the value of the whole magnetic field declines heavily with increasing radial gaps. When it comes to axial gaps, the effect is different. As depicted in Fig. 9(b), only the peak value of the flux field falls with these gaps. In the contrary, the central area of the flux distribution is not affected by g_{ax}. Eventually, the average value of the magnetic flux under the influence of axial gaps is much higher than that of radial gaps with the same gap thickness. Similar simulation results could also be drawn by the FEM results as shown in Fig. 10, which have verified the conclusion of the proposed model.

Comparing radial gaps with axial gaps, the former have a more significant impact on the radial flux density, and the

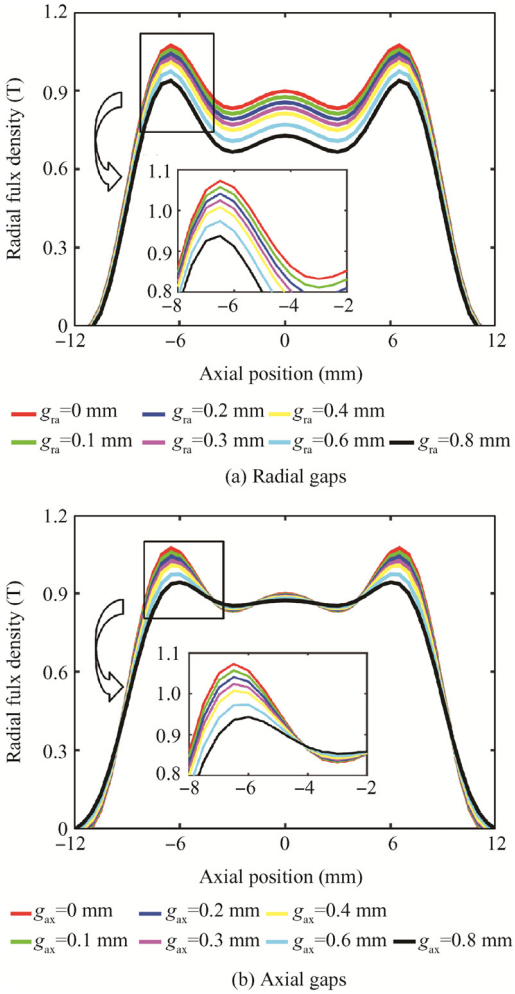

Fig. 9 Effect of gaps on radial flux density analytically.

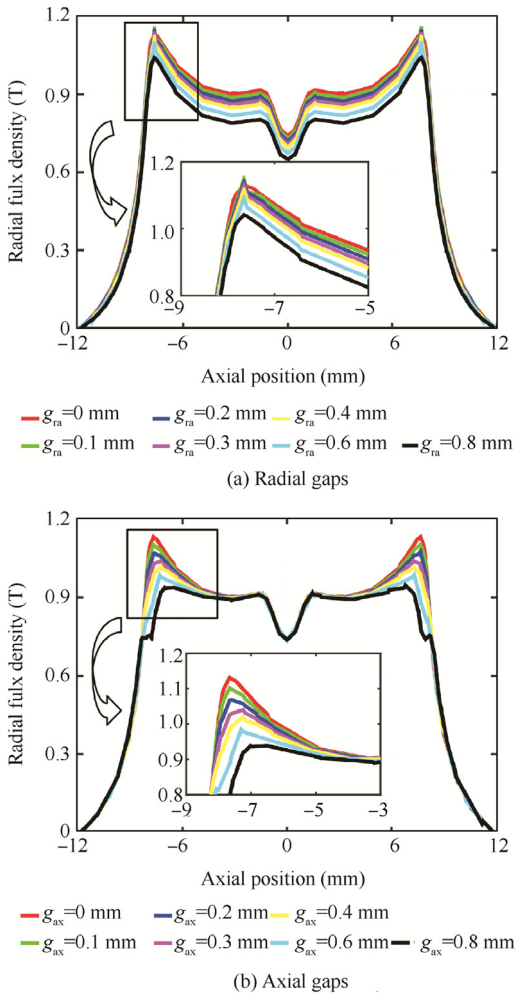

Fig. 10 Effect of gaps on radial flux density by FEM.

negative effect could decrease the energy density of the magnet flied in the air-gap, as well as the power density in the TMMLOM.

4.2.2. Effect of the radial and axial gaps on the thrust

Using the validated model, the relationship between the thrust and mover gaps is further investigated. Fig. 11 reflect the influence of gaps in a normal coils winding.

Assign the current as a constant of 2 A, and the result shows that the thrust varies with the mover position. When the stoke distance is less than 2 mm, the thrust is approximate to a stable value. Nevertheless, if the mover moves further, the thrust would decrease gradually. Because the width of radial magnetized PMs is 16 mm, the width of coils in a winding is 12 mm. The mover moves only in a range of plus and minus 2 mm, so the thrust would not decline, and the stable stroke could be defined as

$$S_s = \frac{\tau_{ra}}{2\tau_w} \tag{25}$$

The radial and axial gaps are another aspect of causes, which lead to a thrust loss. As illustrated in Fig. 11, both types of gaps lead to an overall drop of the thrust curve, and it declines faster in the effect of radial gaps compared with that of

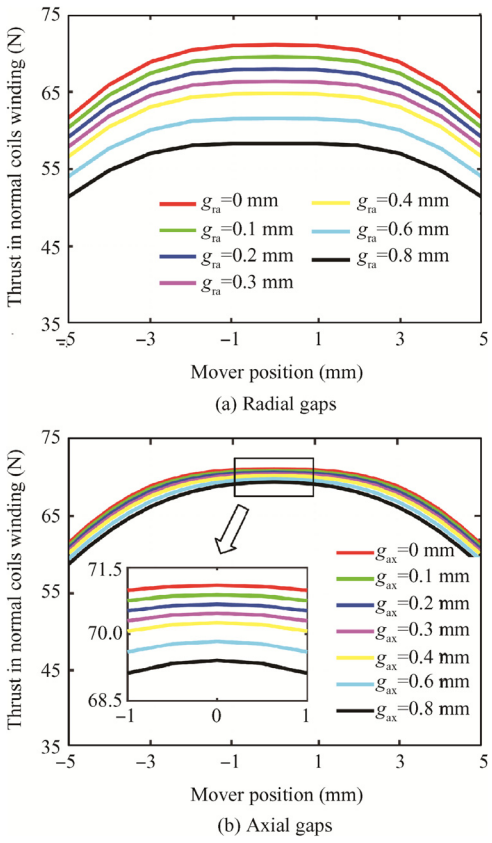

Fig. 11 Effect of gaps on thrust in normal coils winding.

axial gaps. This result agrees well with the distribution of the flux density, for the output force is directly proportional to magnet remanence of permanent magnets B_{re}.

Fig. 12 are the thrust outputs affected by gaps in an end coils winding. The thrust curves of end coils are no more asymmetrical like those in normal coils. The reason is the unsymmetrical distribution of the flux density generated by end PMs. Both of the two end coils have an opposite force trend, which results in the approximate symmetry in dual end coils.

The effect of mover gaps in end coils is unsymmetrical, either. The attenuation is obvious in a positive stoke and unobvious in a negative stoke. As the end coils are not in a strong magnetic area, the thrust as well as the decrement of the thrust drops heavily in the minus mover position. The other effect is the same as that in normal coils.

The total thrust of the TMMLOM is shown in Fig. 13. For the reason that the total force depends mostly on the normal coils, the thrust property is similar to that with the normal coils. Hence, the total thrust of the motor is much more sensitive to the radial gaps than the axial gaps.

5. Comparison with experimental results

He et al. measured the radial flux density of a TMMLOM prototype.[37] She also built an FEM and lumped magnetic circuit model to describe the radial flux density in the air-gap. The error of her analytical model is much greater than that of the FEM results. Her experiment results and FEM calculations are presented in Fig. 14. The radial flux density marked black

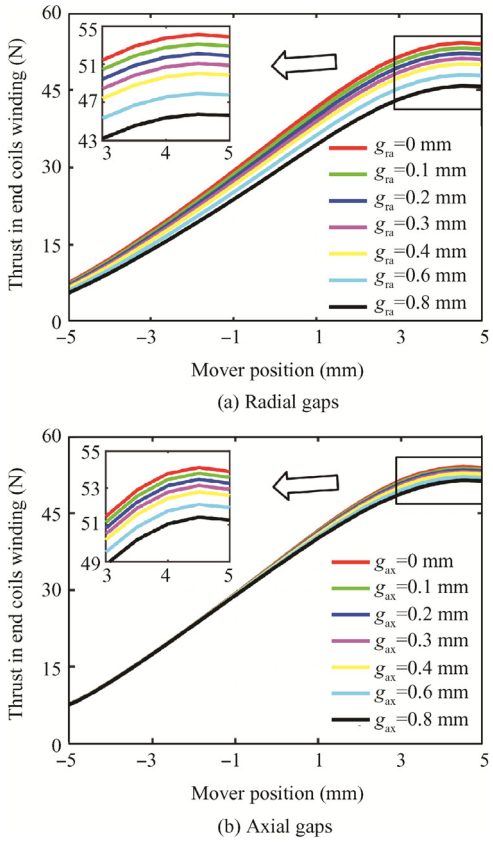

Fig. 12 Effect of gaps on thrust in end coils winding.

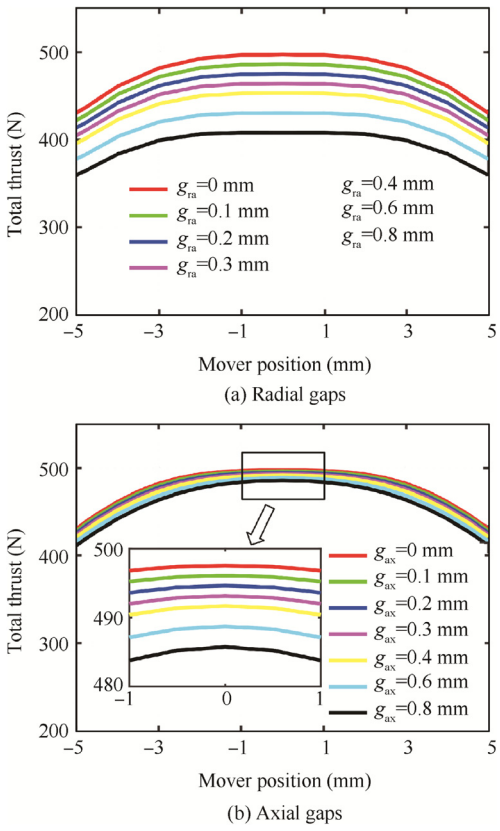

Fig. 13 Effect of gaps on total thrust.

was measured by a Gauss meter with the mover assembled inside the stator. From the figure, the magnetic field intensity of the amaranthine curve is obviously higher than the experimental points. Using the model proposed in this paper to express the magnet field, the analytical results without gaps are close to the FEM curve, which didn't take the mover gaps into account. When taking the gaps into consideration, the mean value is close to the measured data, as shown in the red curve whose axial gap is 0.2 mm and radial gap is 0.5 mm. There still exist some errors because of the stator slot. The comparison confirms the rationality and accuracy of the proposed model.

6. Conclusions

This paper studies the effects of mover gaps in a TMMLOM on the distribution of the magnetic flux density and the output thrust. An analytical model is proposed considering radial and axial gaps, and its performance is validated through FEM experiments.

Based on this approach, both radial and axial gaps would weaken the performance of the TMMLOM. Radial gaps would lead to a comprehensive damping in the radial flux density in the air-gap, while the axial mover only decreases that at the end of the radial polarized magnet. Besides, 85% of the thrust in the motor is produced by normal coils, so the effect of gaps on the total force is similar to that of normal coils. In addition, the existence of radial gaps may cause a thrust decay 5 times as much as that influenced by axial gaps. Thus,

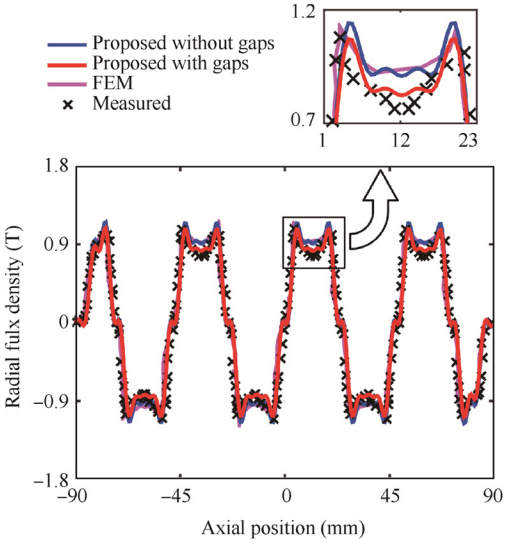

Fig. 14 Comparison with experimental results.

in the process of designing and manufacturing TMMLOMs, it is noticeable to pay more attention to limit the thickness of radial gaps than to axial ones.

Acknowledgements

The authors would like to appreciate the supports of National Basic Research Program of China (973 Program) (No.

2014CB046402), National Natural Science Foundation of China (Nos. 51620105010, 51575019, 51675019, 51505015), and 111 Program of China.

Appendix A

Because the curl of any scalar function's (f) gradient is always equal to zero, we could have

$$\nabla \times \boldsymbol{A}_i = \nabla \times (\boldsymbol{A}_i + \nabla f) \tag{A1}$$

which indicates that $\boldsymbol{A}_i$ may have multiple solutions. To uniquely determine its value, Coulomb gauge, $\nabla \cdot \boldsymbol{A}_i = 0$, is applied as a constraint. Hence, we could have

$$\nabla \times \boldsymbol{B}_i = \nabla \times (\nabla \times \boldsymbol{A}_i) = \nabla(\nabla \cdot \boldsymbol{A}_i) - \nabla^2 \boldsymbol{A}_i = -\nabla^2 \boldsymbol{A}_i \tag{A2}$$

The combination of Maxwell's equations and Eq. (1) gives

$$\nabla \times \boldsymbol{B}_{\mathrm{I}} = \nabla \times \mu_0 \boldsymbol{H}_{\mathrm{I}} = \mu_0 \boldsymbol{J} \tag{A3}$$

Substituting Eq. (A2) into Eq. (A3) yields

$$\nabla^2 \boldsymbol{A}_{\mathrm{I}} = -\mu_0 \boldsymbol{J} \tag{A4}$$

where $\boldsymbol{J}$ (A/m^2) is the current density in the field. In the air–gap of a linear oscillating motor, $\boldsymbol{J} = \boldsymbol{0}$. Therefore, the Laplace's equation for Region I is obtained as

$$\nabla^2 \boldsymbol{A}_{\mathrm{I}} = \boldsymbol{0} \tag{A5}$$

Similarly, the Laplace equation for Region III is derived as

$$\nabla^2 \boldsymbol{A}_{\mathrm{III}} = \boldsymbol{0} \tag{A6}$$

In Region II, the combination of Maxwell's equations and Eq. (1) gives

$$\nabla \times \boldsymbol{B}_{\mathrm{II}} = \mu_0 \mu_{\mathrm{rII}} \boldsymbol{J} + \mu_0 \nabla \times \boldsymbol{M} \tag{A7}$$

For $\boldsymbol{J} = \boldsymbol{0}$, Eqs. (A2) and (A7) obtain the Poisson equation analogously for Region II as

$$\nabla^2 \boldsymbol{A}_{\mathrm{II}} = -\mu_0 \nabla \times \boldsymbol{M} \tag{A8}$$

Appendix B

Considering that expression $A'_{i,\mathrm{ci}}$ is any order of Fourier series of $A_{i,\mathrm{ci}}$, since $A_{i,\mathrm{ci}}$ is only a function of r and θ, we could assume that

$$A'_{i,\mathrm{ci}} = R_i(r) Z_i(z) \tag{B1}$$

where r is the unique variable of $R_i(r)$ and z the unique variable of $Z_i(z)$ according to the method of variable separation.

General solution to Laplace equation

The Laplace Eqs. (A5) and (A6) in cylindrical coordinates can be simplified as

$$\begin{aligned}\nabla^2 \boldsymbol{A} &= \nabla^2(A_{\mathrm{ra}} \boldsymbol{e}_{\mathrm{ra}}) + \nabla^2(A_{\mathrm{ci}} \boldsymbol{e}_{\mathrm{ci}}) + \nabla^2(A_{\mathrm{ax}} \boldsymbol{e}_{\mathrm{ax}}) \\ &= \nabla^2(A_{\mathrm{ci}} \boldsymbol{e}_{\mathrm{ci}}) = \boldsymbol{0}\end{aligned} \tag{B2}$$

$$\begin{aligned}\nabla^2(A_{\mathrm{ci}} \boldsymbol{e}_{\mathrm{ci}}) = &-\frac{2}{r^2} \cdot \frac{\partial A_{\mathrm{ci}}}{\partial \theta} \boldsymbol{e}_{ra} \\ &+ \left(\frac{\partial^2 A_{\mathrm{ci}}}{\partial r^2} + \frac{1}{r} \cdot \frac{\partial A_{\mathrm{ci}}}{\partial r} + \frac{\partial^2 A_{\mathrm{ci}}}{\partial z^2} + \frac{2}{r^2} \cdot \frac{\partial A_{\mathrm{ci}}}{\partial \theta} - \frac{A_{\mathrm{ci}}}{r^2} \right) \boldsymbol{e}_{\mathrm{ci}} = 0\end{aligned} \tag{B3}$$

For the magnetic field distribution of a tubular linear oscillating motor is axially symmetric, the expression becomes

$$\left(\frac{\partial^2 A_{\mathrm{ci}}}{\partial r^2} + \frac{1}{r} \cdot \frac{\partial A_{\mathrm{ci}}}{\partial r} - \frac{A_{\mathrm{ci}}}{r^2} + \frac{\partial^2 A_{\mathrm{ci}}}{\partial z^2} \right) \boldsymbol{e}_{\mathrm{ci}} = 0 \tag{B4}$$

namely,

$$\frac{\partial^2 A'_{\mathrm{ci}}}{\partial r^2} + \frac{1}{r} \cdot \frac{\partial A'_{\mathrm{ci}}}{\partial r} - \frac{A'_{\mathrm{ci}}}{r^2} + \frac{\partial^2 A'_{\mathrm{ci}}}{\partial z^2} = 0 \tag{B5}$$

where $i = \mathrm{I}, \mathrm{III}$ and A'_{ci} is any order of Fourier series of A_{ci}. Substituting Eq. (B1) into Eq. (B4) yields

$$\frac{1}{R_i(r)} \cdot \frac{\partial^2 R_i(r)}{\partial r^2} + \frac{1}{R_i(r) r} \cdot \frac{\partial R_i(r)}{\partial r} - \frac{1}{r^2} + \frac{1}{Z_i(z)} \cdot \frac{\partial^2 Z_i(z)}{\partial z^2} = 0 \tag{B6}$$

where r and z are independent variables, and the last term as a function of z must be a constant. Therefore, the following formula is established:

$$\frac{1}{Z_i(z)} \cdot \frac{\partial^2 Z_i(z)}{\partial z^2} = \lambda^2 \tag{B7}$$

Then Eq. (B5) can be written as

$$\frac{1}{R_i(r)} \cdot \frac{\partial^2 R_i(r)}{\partial r^2} + \frac{1}{R_i(r) r} \cdot \frac{\partial R_i(r)}{\partial r} + \lambda^2 - \frac{1}{r^2} = 0 \tag{B8}$$

Eq. (B6) becomes

$$\frac{\partial^2 Z_i(z)}{\partial z^2} - \lambda^2 Z_i(z) = 0 \tag{B9}$$

So Eq. (B5) equals to

$$\begin{cases} \frac{\partial^2 Z_i(z)}{\partial z^2} - \lambda^2 Z_i(z) = 0 \\ \frac{1}{R_i(r)} \cdot \frac{\partial^2 R_i(r)}{\partial r^2} + \frac{1}{R_i(r) r} \cdot \frac{\partial R_i(r)}{\partial r} + \lambda^2 - \frac{1}{r^2} = 0 \end{cases} \tag{B10}$$

and there are three possible solutions according to the variation of λ^2.

When $\lambda^2 = 0$, the following equations are obtained:

$$\begin{cases} \frac{\partial^2 Z_i(z)}{\partial z^2} = 0 \\ r^2 \frac{\partial^2 R_i(r)}{\partial r^2} + r \frac{\partial R_i(r)}{\partial r} - R_i(r) = 0 \end{cases} \tag{B11}$$

The general solution to Eq. (B11) is

$$\begin{cases} Z_i(z) = C_0 + C_1 z \\ R_i(r) = C_2 r + \frac{C_3}{r} \end{cases} \tag{B12}$$

where C_0, C_1, C_2, C_3 are constants. Thus

$$A'_{i,\mathrm{ci}} = R_i(r) Z_i(z) = (C_0 + C_1 z)(C_2 r + \frac{C_3}{r}) \tag{B13}$$

For $A'_{i,\mathrm{ci}}$ should be a periodic function of z, Eq. (B13) is not a valid solution of $A'_{i,\mathrm{ci}}$.

When $\lambda^2 > 0$, the following equations are obtained:

$$\begin{cases} \frac{\partial^2 Z_i(z)}{\partial z^2} - \lambda^2 Z_i(z) = 0 \\ \frac{\partial^2 R_i(r)}{\partial (\lambda r)^2} + \frac{1}{\lambda r} \cdot \frac{\partial R_i(r)}{\partial (\lambda r)} + (1 - \frac{1}{(\lambda r)^2}) R_i(r) = 0 \end{cases} \tag{B14}$$

The general solution to Eq. (B11) is

$$\begin{cases} Z_i(z) = C_0 \mathrm{e}^{\lambda z} + C_1 \mathrm{e}^{-\lambda z} \\ R_i(r) = C_2 J_1(\lambda r) + C_3 Y_1(\lambda r) \end{cases} \tag{B15}$$

where C_0, C_1, C_2, C_3 are constants, $J_n(x)$ is the Bessel function of the first kind of order n, $Y_n(x)$ the Bessel function of the second kind of order n, and $\Gamma(x)$ the Gamma function, which are defined as

$$\begin{cases} J_n(x) = \sum_{m=0}^{\infty} \frac{(-1)^m}{m!\Gamma(m+n+1)} \left(\frac{x}{2}\right)^{2m+n} \\ Y_n(x) = \frac{J_n(x)\cos(n\pi) - J_{-n}(x)}{\sin(n\pi)} \qquad x \in \mathbf{R} \\ \Gamma(x) = \int_0^{\infty} \mathrm{e}^{-t} t^{x-1} \mathrm{d}t \end{cases} \tag{B16}$$

Thus

$$\begin{aligned} A'_{i,\mathrm{ci}} &= R_i(r) Z_i(z) \\ &= (C_0 \mathrm{e}^{\lambda z} + C_1 \mathrm{e}^{-\lambda z})[C_2 J_1(\lambda r) + C_3 Y_1(\lambda r)] \end{aligned} \tag{B17}$$

For $A'_{i,\mathrm{ci}}$ should be a periodic function of z, Eq. (B17) is not a valid solution of $A'_{i,\mathrm{ci}}$.

When $\lambda^2 < 0$, let $\lambda = \mathrm{j}m_k$, where j is the imaginary unit. The following equations are obtained:

$$\begin{cases} \frac{\partial^2 Z_i(z)}{\partial z^2} + m_k^2 Z_i(z) = 0 \\ \frac{\partial^2 R_i(r)}{\partial (m_k r)^2} + \frac{1}{\lambda r} \cdot \frac{\partial R_i(r)}{\partial (m_k r)} - \left(1 + \frac{1}{(m_k r)^2}\right) R_i(r) = 0 \end{cases} \tag{B18}$$

The general solution to Eq. (B18) is

$$\begin{cases} Z_i(z) = C_0 \cos(m_k z) + C_1 \sin(m_k z) \\ R_i(r) = C_2 I_1(m_k r) + C_3 K_1(m_k r) \end{cases} \tag{B19}$$

Thus

$$\begin{aligned} A'_{i,\mathrm{ci}} = R_i(r) Z_i(z) = [C_4 I_1(m_k r) + C_5 K_1(m_k r)]\cos(m_k z) \\ + [C_6 I_1(m_k r) + C_7 K_1(m_k r)]\sin(m_k z) \end{aligned} \tag{B20}$$

where C_4, C_5, C_6, C_7 are constants. In this case, $A'_{i,\mathrm{ci}}$ is a periodic function of z. Hence, Eq. (B20) is probably a solution of Laplace's equation.

Eq. (7) in cylindrical coordinates is expressed as

$$\boldsymbol{B}_i = \left(-\frac{\partial A_{i,\mathrm{ci}}}{\partial z}\right) \boldsymbol{e}_{\mathrm{ra}} + \frac{1}{r}\left(\frac{\partial (r A_{i,\mathrm{ci}})}{\partial r}\right) \boldsymbol{e}_{\mathrm{ax}} \tag{B21}$$

Considering the constraint of symmetry at $z = 0$, we have the radial component of the flux density $B_{\mathrm{ra}|z=0} = 0$. Moreover, Substituting Eq. (B20) into Eq. (B21) gives

$$\begin{aligned} \boldsymbol{B}_{\mathrm{I}} = \sum_{k=1}^{\infty} \{ & m_k \{ [C_4 I_1(m_k r) + C_5 K_1(m_k r)]\sin(m_k z) \\ & - [C_6 I_1(m_k r) + C_7 K_1(m_k r)]\cos(m_k z) \} \boldsymbol{e}_{\mathrm{ra}} \\ & + \frac{1}{r}\left(\frac{\partial (r A_{\mathrm{I},\mathrm{ci}})}{\partial r}\right) \boldsymbol{e}_{\mathrm{ax}} \} \end{aligned} \tag{B22}$$

Thus we draw the conclusion that

$$\begin{cases} C_6 = 0 \\ C_7 = 0 \end{cases} \tag{B23}$$

Therefore, the general solution to the Laplace's Eq. (B6) is

$$A_{i,\mathrm{ci}} = \sum_{k=1}^{\infty} \{ [a_{i,k} I_1(m_k r) + b_{i,k} K_1(m_k r)]\cos(m_k z) \} \tag{B24}$$

where $i = \mathrm{I}, \mathrm{III}$ and $a_{i,k}, b_{i,k}$ are constants.

General solution to Poisson equation

The Poisson Eq. (A8) in cylindrical coordinates can be simplified as

$$\left(\frac{\partial^2 A_{\mathrm{II},\mathrm{ci}}}{\partial r^2} + \frac{1}{r} \cdot \frac{\partial A_{\mathrm{II},\mathrm{ci}}}{\partial r} - \frac{A_{\mathrm{II},\mathrm{ci}}}{r^2} + \frac{\partial^2 A_{\mathrm{II},\mathrm{ci}}}{\partial z^2}\right) \boldsymbol{e}_{\mathrm{ci}} = -\mu_0 \frac{\partial M_{\mathrm{ra}}}{\partial z} \boldsymbol{e}_{\mathrm{ci}} \tag{B25}$$

Substituting Eq. (4) into Eq. (B25) yields

$$\begin{aligned} & \frac{\partial^2 A_{\mathrm{II},\mathrm{ci}}}{\partial r^2} + \frac{1}{r} \cdot \frac{\partial A_{\mathrm{II},\mathrm{ci}}}{\partial r} - \frac{A_{\mathrm{II},\mathrm{ci}}}{r^2} + \frac{\partial^2 A_{\mathrm{II},\mathrm{ci}}}{\partial z^2} \\ & = -\mu_0 \sum_{k=1}^{\infty} m_k b_k \cos(m_k z) \end{aligned} \tag{B26}$$

Similarly, the general solution to the corresponding homogeneous equation of the Poisson Eq. (B26) is

$$\sum_{k=1}^{\infty} S(r,z) = \sum_{k=1}^{\infty} R_{\mathrm{II}}(r) Z_{\mathrm{II}}(z) \tag{B27}$$

Assuming that $\sum_{k=1}^{\infty} S(r,z) = \sum_{k=1}^{\infty} R_{\mathrm{II}}(r) Z_{\mathrm{II}}(z)$ is a particular solution of the Poisson equation, the general solution to the Poisson equation is obtained as

$$A_{\mathrm{II},\mathrm{ci}} = \sum_{k=1}^{\infty} \{ [a_{\mathrm{II},k} I_1(m_k r) + b_{\mathrm{II},k} K_1(m_k r)]\cos(m_k z) + S_k(r,z) \} \tag{B28}$$

Substituting $\sum_{k=1}^{\infty} S(r,z) = \sum_{k=1}^{\infty} R_{\mathrm{II}}(r) Z_{\mathrm{II}}(z)$ into Eq. (B26) gives

$$\begin{aligned} & \frac{1}{R_{\mathrm{II},k}(r)} \cdot \frac{\partial^2 R_{\mathrm{II},k}(r)}{\partial r^2} + \frac{1}{R_{\mathrm{II},k}(r) r} \cdot \frac{\partial R_{\mathrm{II},k}(r)}{\partial r} - \frac{1}{r^2} + \frac{1}{Z_{\mathrm{II},k}(z)} \\ & \cdot \frac{\partial^2 Z_{\mathrm{II},k}(z)}{\partial z^2} \\ & = \frac{-\mu_0 m_k b_k \cos(m_k z)}{R_{\mathrm{II},k}(r) Z_{\mathrm{II},k}(z)} \end{aligned} \tag{B29}$$

Let $\frac{1}{Z_{\mathrm{II},k}(z)} \cdot \frac{\partial^2 Z_{\mathrm{II},k}(z)}{\partial z^2} = -m_k^2$, i.e.,

$$Z_{\mathrm{II}}(z) = \cos(m_k z) \tag{B30}$$

Substituting Eq. (B30) into Eq. (B29) yields

$$\begin{aligned} & (m_k r)^2 \frac{\partial^2 \left(\frac{R_{\mathrm{II},k}(r)}{P_k}\right)}{\partial (m_k r)^2} + m_k r \frac{\partial \left(\frac{R_{\mathrm{II},k}(r)}{P_k}\right)}{\partial (m_k r)} \\ & - ((m_k r)^2 + 1)\left(\frac{R_{\mathrm{II},k}(r)}{P_k}\right) = \frac{2(m_k r)^2}{\pi} \end{aligned} \tag{B31}$$

where $P_k = -\frac{\mu_0 \pi b_k}{2 m_k}$. The general solution to the modified Struve differential Eq. (B31) is

$$R_{\mathrm{II}}(r) = P_k L_1(m_k r) \tag{B32}$$

where $H_n(x)$ are the Struve functions of order n and $L_n(x)$ the modified Struve functions of order n.

$$\begin{cases} H_n(x) = \left(\frac{x}{2}\right)^{n+1} \sum_{m=0}^{\infty} \frac{(-1)^m \left(\frac{x}{2}\right)^{2m}}{\Gamma\left(m+\frac{3}{2}\right)\Gamma\left(m+n+\frac{3}{2}\right)} \\ L_n(x) = -\mathrm{j}\mathrm{e}^{-n\pi \mathrm{j}/2} H_n(\mathrm{j}x) \end{cases} \tag{B33}$$

Hence, the particular solution of the Poisson equation is

$$S_k(r,z) = R_{\mathrm{II},k}(r)Z_{\mathrm{II},k}(z) = P_k L_1(m_k r)\cos(m_k z) \tag{B34}$$

Substituting Eq. (B34) into Eq. (B28) derives the general solution to the Poisson equation as

$$A_{\mathrm{II,ci}} = \sum_{k=1}^{\infty}[a_{\mathrm{II},k}I_1(m_k r) + b_{\mathrm{II},k}K_1(m_k r) + P_k L_1(m_k r)]\cos(m_k z) \tag{B35}$$

Appendix C

Submitting Eqs. (12) and (13) into Eq. (14), we can yield the following equation:

$$\begin{bmatrix} I_0(m_kR_{se}) & -K_0(m_kR_{se}) & 0 & 0 & 0 & 0 \\ I_1(m_kR_m) & K_1(m_kR_m) & -I_1(m_kR_m) & -K_1(m_kR_{\mathrm{m}}) & 0 & 0 \\ I_0(m_kR_m) & -K_0(m_kR_m) & -I_0(m_kR_{\mathrm{m}}) & K_0(m_kR_m) & 0 & 0 \\ 0 & 0 & I_1(m_kR_{\mathrm{p}}) & K_1(m_kR_p) & -I_1(m_kR_p) & -K_1(m_kR_{\mathrm{p}}) \\ 0 & 0 & I_0(m_kR_{\mathrm{p}}) & -K_0(m_kR_{\mathrm{p}}) & -I_0(m_kR_{\mathrm{p}}) & K_0(m_kR_{\mathrm{p}}) \\ 0 & 0 & 0 & 0 & I_0(m_kR_h) & -K_0(m_kR_{\mathrm{h}}) \end{bmatrix} \begin{bmatrix} a_{\mathrm{I},k} \\ b_{\mathrm{I},k} \\ a_{\mathrm{II},k} \\ b_{\mathrm{II},k} \\ a_{\mathrm{III},k} \\ b_{\mathrm{III},k} \end{bmatrix} = \begin{bmatrix} 0 \\ P_kL_1(m_kR_{\mathrm{m}}) \\ P_kL_0(m_kR_{\mathrm{m}}) - \frac{\mu_0 b_k}{m_k} \\ -P_kL_1(m_kR_{\mathrm{p}}) \\ -P_kL_0(m_kR_{\mathrm{p}}) + \frac{\mu_0 b_k}{m_k} \\ 0 \end{bmatrix} \tag{C1}$$

The solutions of Eq. (C1) fix the undetermined coefficients in Eqs. (12) and (13).

References

1. Ebihara D, Watada M. Development of a single-winding linear oscillatory actuator. *IEEE Trans Magn* 1992;**28**(5):3030–2.
2. Watada M, Yanashima K, Oishi Y, Ebihara D, Dohmeki H. Improvement on characteristics of linear oscillatory actuator for artificial hearts. *IEEE Trans Magn* 1993;**29**(6):3361–3.
3. Redlich R. A summary of twenty years experience with linear motors and alternators. *Proceedings of linear divers for industry applications*; 1995 May 31–June 2 Nagasaki, Japan. 1995. p. 1–7.
4. Boldea I, Nasar SA. Linear electric actuators and generators*Electric machines and drives conference*. Cambridge, UK. Piscataway, NJ: IEEE Press; 1997. p. 5.
5. Lee HK, Song GY, Park JS, Hong EP, Jung WH. Development of the linear compressor for a household refrigerator. *Proceedings of fifteenth international compressor engineering conference*; 2000 July 25–28; West Lafayette, USA; 2000. p. 31–38.
6. Lee H, Jeong SS, Lee CW, Lee HK. Linear compressor for air-conditioner. *Proceedings of the international compressor engineering conference*; 2004 July 12–15; West Lafayette, USA. 2004. p. C047.
7. Liang HS, Jiao ZX, Yan L, Zhao LF, Wu S, Li Y. Design and analysis of a tubular linear oscillating motor for directly-driven eha pump. *Sens Actuators A – Phys* 2014;**210**:107–18.
8. Wang TY, Liang HS, Jiao ZX, He P, Yan L. Dynamics modeling and load analysis of linear motor for leha system. *Proceedings of fluid power and mechatronics (FPM)*; 2015 Aug 5–7; Harbin, China. 2015. p. 1128–33.
9. Wang ZM, Jiao ZX, Li Y. Analysis, design and simulation of a collaborative rectification hydraulic pump. *Proceedings of guidance, navigation and control conference (CGNCC)*, 2014 Aug 8–10; Beijing, China. 2014. p. 2065–70.
10. Kim TH, Lee HW, Kim YH, Lee J. Development of a flux concentration-type linear oscillatory actuator. *IEEE Trans Magn* 2004;**40**(4):2092–4.
11. Tutelea LN, Kim MC, Topor M, Ju L, Boldea I. Linear permanent magnet oscillatory machine: Comprehensive modeling for transients with validation by experiments. *IEEE Trans Industr Electron* 2008;**55**(2):492–500.
12. Kim YK, Gu BG, Rhyu SH, Jung IS. Analysis and design of slotless tubular linear actuator for high performance on the eco-pedal system of vehicles. *Int J Appl Electromagnet Mech* 2012;**39**(1):817–23.
13. Kim YK, Gu BG, Jung IS, Won SH, Hur J. Analysis and design of slotted tubular linear actuator for the eco-pedal system of a vehicle. *IEEE Trans Magn* 2012;**48**(2):939–42.
14. Wang JB, Jewell GW, Howe D. General framework for the analysis and design of tubular linear permanent magnet machines. *IEEE Trans Magn* 1999;**35**(3):1986–2000.
15. Bianchi N, Bolognani S, Corte DD, Tonel F. Tubular linear permanent magnet motors: An overall comparison. *IEEE Trans Ind Appl* 2003;**39**(2):466–75.
16. Wang JB, Howe D, Lin ZY. Comparative study of winding configurations of short-stroke, single phase tubular permanent magnet motor for refrigeration applications. *Proceedings of the 42nd IEEE IAS annual meeting*; 2007 Sept 23–27; New Orleans, USA. 2007. p. 31123–8.
17. Wang JB, Howe D, Lin ZY. Comparative studies on linear motor topologies for reciprocating vapor compressors. *2007 IEEE international electric machines & drives conference*; 2007 May 3–5; Antalya, Turkey. 2007. p. 364–9.
18. Wang JB, Lin ZY, Howe D. Analysis of a short-stroke, single-phase, quasi-halbach magnetised tubular permanent magnet motor for linear compressor applications. *IET Electr Power Appl* 2008;**2**(3):193–200.
19. Wang JB, Howe D, Lin ZY. Design optimization of short-stroke single-phase tubular permanent-magnet motor for refrigeration applications. *IEEE Trans Industr Electron* 2010;**57**(1):327–34.
20. Zhu ZQ, Chen X, Howe D, Iwasaki S. Electromagnetic modeling of a novel linear oscillating actuator. *IEEE Trans Magn* 2008;**44**(11):3855–8.
21. Chen X, Zhu ZQ, Howe D, Dai JS. Comparative study of alternative permanent magnet linear oscillating actuators. *Proceedings of 2008 international conference on electrical machines and systems*. 2008 Oct 17–20; Sapporo, Japan. 2008. p. 2826–31.
22. Zhu ZQ, Chen X. Analysis of an E-core interior permanent magnet linear oscillating actuator. *IEEE Trans Magn* 2009;**45**(10):4384–7.
23. Chen X, Zhu ZQ, Howe D. Modeling and analysis of a tubular oscillating permanent-magnet actuator. *IEEE Trans Ind Appl* 2009;**45**(6):1961–70.
24. Chen X, Zhu ZQ. Analytical determination of optimal split ratio of e-core permanent magnet linear oscillating actuators. *IEEE Trans Ind Appl* 2011;**47**(1):25–33.
25. Wang TY, He P, Yan L, Jiao ZX. Modeling, simulation and experiment study of electromagnetic performance for E-type series linear oscillating motor. *Proceedings of IEEE international confer-*

ence on advanced intelligent mechatronics; 2015 Jul 7–11; Busan, Korea. 2015. p. 607–12.
26. Jiao ZX, Wang TY, Yan L. Design of a tubular linear oscillating motor with novel compound halbach magnet array. *IEEE/ASME Trans Mechatron* 2016;**22**(1):498–508.
27. Wang JB, Howe D. Tubular modular permanent-magnet machines equipped with quasi-halbach magnetized magnets-part I: Magnetic field distribution, emf, and thrust force. *IEEE Trans Magn* 2005;**41**(9):2470–8.
28. Wang TY, Yan L, Jiao ZX, He P. Analytical modeling of linear oscillating motor with a mixed method considering saturation effect. *Sens Actuators A – Phys* 2015;**234**:375–83.
29. Jang S, Choi J, You D. Dynamic performance of tubular linear actuator with halbach array and mechanical spring driven by pwm inverter. *IEEE Trans Magn* 2006;**42**(10):3518–20.
30. Karunanithi R, Jacob S, Singh GAS, Damu C, Das M. Development of moving magnet type linear motor for dual piston compressor for pulse tube cryocooler. *Adv Cryogenic Eng: Trans* 2012;**1434**(1):525–31.
31. Nowak L. Dynamic FE analysis of quasi-axisymmetrical electromechanical converters. *IEEE Trans Magn* 1994;**30**(5):3268–71.
32. Sadowski N, Carlson R, Beckert AM, Bastos JPA. Dynamic modeling of a newly designed linear actuator using 3d edge elements analysis. *IEEE Trans Magn* 1996;**32**(3):1633–6.
33. Tomczuk B, Sobol M. A field-network model of a linear oscillating motor and its dynamics characteristics. *IEEE Trans Magn* 2005;**41**(8):2362–7.
34. Ji JH, Yan SJ, Zhao WX, Liu GH, Zhu XY. Minimization of cogging force in a novel linear permanent-magnet motor for artificial hearts. *IEEE Trans Magn* 2013;**49**(7):3901–4.
35. Kim KH, Park HI, Jeong SS, Jang SM, Choi JY. Comparison of characteristics of permanent-magnet linear oscillating actuator according to laminated method of stator core. *IEEE Trans Appl Supercond* 2016;**26**(4):1–4.
36. Wang TY, Jiao ZX, Yan L, Chen CY, Chen IM. Design and analysis of an improved halbach tubular linear motor with non-ferromagnetic mover tube for direct-driven EHA. *Proceedings of IEEE chinese guidance, navigation and control conference*; 2014 Oct 8–10; Yantai, China. 2014. p. 797–802.
37. He P, Jiao ZX, Yan L, Liang HS. Analysis of magnet layout in circumferential and axial direction for halbach PM arrays. *Proceedings of guidance, navigation and control conference*; 2014 Oct 8–10; Yantai, China. 2014. p. 2013–8.
38. Wang TY, Jiao ZX, Yan L, He P. Design of novel double-layer compound stator for tubular linear oscillating motor. *Proceedings of 2015 IEEE 10th conference on industrial electronics and applications (ICIEA)*; 2015 Jun 15–17; Auckland, New Zealand. 2015. p. 1910–5.
39. Xia CL, Guo L, Wang H. Modeling and analyzing of magnetic field of segmented halbach array permanent magnet machine considering gap between segments. *IEEE Trans Magn* 2014;**50**(12):1–9.
40. Gu QS, Gao HZ. Effect of slotting in PM electric machines. *Electr Mach Power Syst* 1985;**10**(4):273–84.
41. Tomczuk B, Schroder G, Waindok A. Finite-element analysis of the magnetic field and electromechanical parameters calculation for a slotted permanent-magnet tubular linear motor. *IEEE Trans Magn* 2007;**43**(7):3229–36.